OSAS-B: A balloon-borne terahertz spectrometer for atomic oxygen in the upper atmosphere

M. Wienold[1], A. Semenov[1], E. Dietz[1], S. Frohmann[1], P. Dern[1], X. Lü[2], L. Schrottke[2], K. Biermann[2], B. Klein[3], H.-W. Hübers[1,4]

[1]German Aerospace Center (DLR), Institute of Optical Sensor Systems, Rutherfordstr. 2, 12489 Berlin, Germany

[2]Paul-Drude-Institut für Festkörperelektronik, Leibniz-Institut im Forschungsverbund Berlin e.V., Hausvogteiplatz 5–7, 10117 Berlin, Germany

[3]Max-Planck-Institut für Radioastronomie, Auf dem Hügel 69, 53121 Bonn, Germany

[4]Humboldt-Universität zu Berlin, Department of Physics, Newtonstr. 15, 12489 Berlin, Germany

Abstract—The oxygen spectrometer for atmospheric science on a balloon (OSAS-B) is the first 4.7-THz heterodyne spectrometer on a stratospheric balloon. It has been developed for remote sensing of the 4.7-THz emission of neutral atomic oxygen in the mesosphere and lower thermosphere of the Earth. OSAS-B comprises a heterodyne receiver based on a hot-electron bolometer mixer and a quantum-cascade laser as local oscillator. The high sensitivity of the superconducting detector and the large resolving power of approximately 1×10^7 enable the detection of subtle signatures of radiation transport and high-altitude winds in the measured spectra. The first flight of the instrument took place on September 7th, 2022 from Esrange, Sweden.

Index Terms—heterodyne receiver, hot-electron bolometer, quantum-cascade laser, terahertz radiation, atomic oxygen, atmospheric measurements

I. INTRODUCTION

Atomic oxygen is one of the dominant species in the mesosphere and lower thermosphere (MLT) of Earth. It is found from 50 km to more than 500 km altitude and plays a major role for the chemistry and energy balance in the MLT region [1], [2], as well as for the corrosion and deceleration of satellites and space debris [3], [4]. Most investigations of atomic oxygen rely on remote sensing. Typically, studies are based on optical transitions in the visible range at 558 nm or 630 nm [5], [6] or indirect conclusions via other species [7]. In both cases, excitation rates and photochemical reaction rates are required to determine the atomic oxygen concentration, which cause an additional uncertainty. The brightest thermally excited transition of neutral atomic oxygen (OI) is the $^3P_1 \rightarrow ^3P_2$ ground state transition at 4.7448 THz. Due to water absorption bands, this line cannot be observed from ground. Recently, the heterodyne receiver GREAT (German REceiver for Astronomy at THz frequencies) on board of SOFIA (Stratospheric Observatory For Infrared Astronomy) enabled spectrally resolved observations of the 4.7-THz transition [8]–[10].

We developed the Oxygen Spectrometer for Atmospheric Science on a Balloon (OSAS-B) to study the 4.7-THz emission of OI in Earth's atmosphere. Advantages of the approach over GREAT/SOFIA are the ability to measure during daytime, at low elevation angles, and with negligible interference from
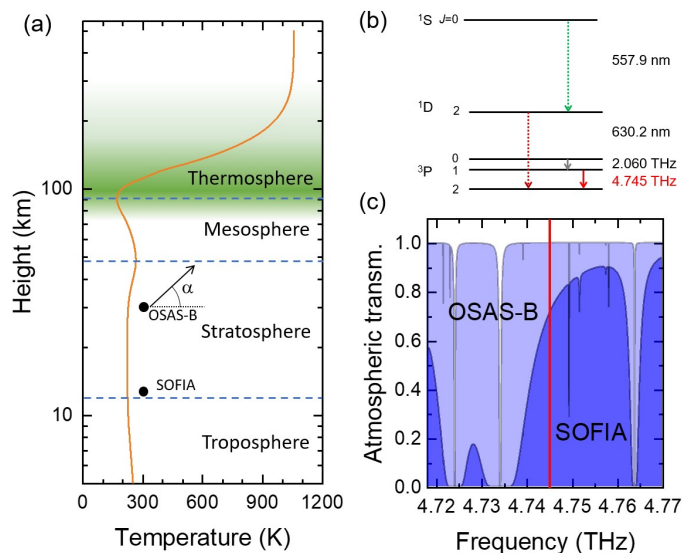

Fig. 1. (a) Typical atmospheric temperature profile and layer definition. Atomic oxygen region in green color. (b) Energy levels and radiative transitions of atomic oxygen (not to scale) [13]. (c) Typical transmission of the atmosphere for a low elevation ($\alpha = 20°$) as for SOFIA at 12 km altitude and OSAS-B at 32 km height.

water absorption bands. However, there are particular challenges for stratospheric balloon instruments such as weight and power limitations, temperatures down to −80 °C during the ascent, as well as the low pressure (< 10 hPa) at flight altitude with an almost complete absence of convective cooling. As an overview, Figures 1(a)–(c) depict the atmospheric structure, the electromagnetic transitions of OI, and the typical transmission of the atmosphere at low elevation for SOFIA and OSAS-B.

In this article, we describe the design and instrument performance of OSAS-B and give an overview of the scientific data and findings from the first flight. A balloon-based mission with a similar technology approach is GUSTO (Galactic/Xtragalactic Ultra-Long Duration Balloon Stratospheric Terahertz Observatory) which focuses on astronomy and which is scheduled for 2023/2024 [11], [12].

II. INSTRUMENT DESIGN AND PERFORMANCE

A. Overview

The OSAS-B instrument was developed for short-to-medium duration flights with a stratospheric balloon in the framework of the European Hemera program [14], [15]. The spectrometer frontend comprises a superconducting hot-electron bolometer (HEB) as the mixer and a quantum-cascade laser (QCL) as the local oscillator (LO). Both components require cryogenic cooling for operation, which is provided by the central optical dewar. Although developed for shorter return flights with 6–12 h duration, the hold-time of the cryogens allows for an observation period of up to two days. The instrument is visualized in Fig. 2(a), with the details of the spectrometer optics shown in Figs. 2(b),(c). The instrument weighs approximately 65 kg including cryogens and consumes 90 W in full operation. For collecting the atmospheric emission and for radiometric calibration, the pointing mirror of the receiver can be turned to the sky from 0° (horizontal) to 60° elevation and to each of the two calibration black bodies (C1, C2). The spatial resolution is approximately 40' and determined by the beam profile of the quasi-optical HEB antenna. The backend of the instrument comprises an amplifier chain at ambient temperature and a digital fast Fourier transform spectrometer (DFFTS) with a resolution of 183 kHz and a bandwidth of 1.5 GHz [16]. Remote control, communication and data storage is handled by a single-board computer (Raspberry Pi 4). An inertial measurement unit including an electronic compass and a camera are used to track the orientation of the instrument during flight.

B. Cryogenic frontend and optics

While the QCL is operated at around 60 K, the HEB requires cooling to 4 K. The cryostat is a customized version of the HDL8 dewar (Infrared Laboratories). It contains a liquid/solid nitrogen stage (4.5 l) for cooling the QCL and the internal cold shield. The 4 K stage is cooled with 5 l of liquid helium and hosts the HEB mixer and the cryogenic low-noise amplifier with a bandwidth of 4 GHz. The cryostat weighs 23/26 kg (empty/filled) and features a hold time of 53 h for the nitrogen, 70 h for the helium, and continuous receiver operation of up to 42 h. For heterodyne detection, the QCL has to pump the HEB mixer with sufficient power at the precise LO frequency. An optical cage system is directly attached to the outer vessel of the cryostat and carries the relay optics for focusing and attenuating the QCL beam. Figure 2(b) depicts a schematic of the cryostat and the relay optics. The optical path comprises a silicon lens, an adjustable mirror, as well as an attenuator unit based on a rotatable and a fixed polarizer. The cryostat windows are made of antireflection-coated Si with 90% transmission. A cold metal mesh low-pass filter in front of the HEB mixer blocks the thermal background (manufactured by QMC, cut-off frequency: 5.1 THz). The atmospheric signal and the QCL beam are combined via a Mylar beam splitter (6 μm foil thickness). The signal transmission at 4.7 THz is 91 % for p-polarized and 64 % for s-polarized light (77 % for circular polarization). The plane pointing mirror with a diameter of 35 mm is directly mounted on the axis of a stepper motor
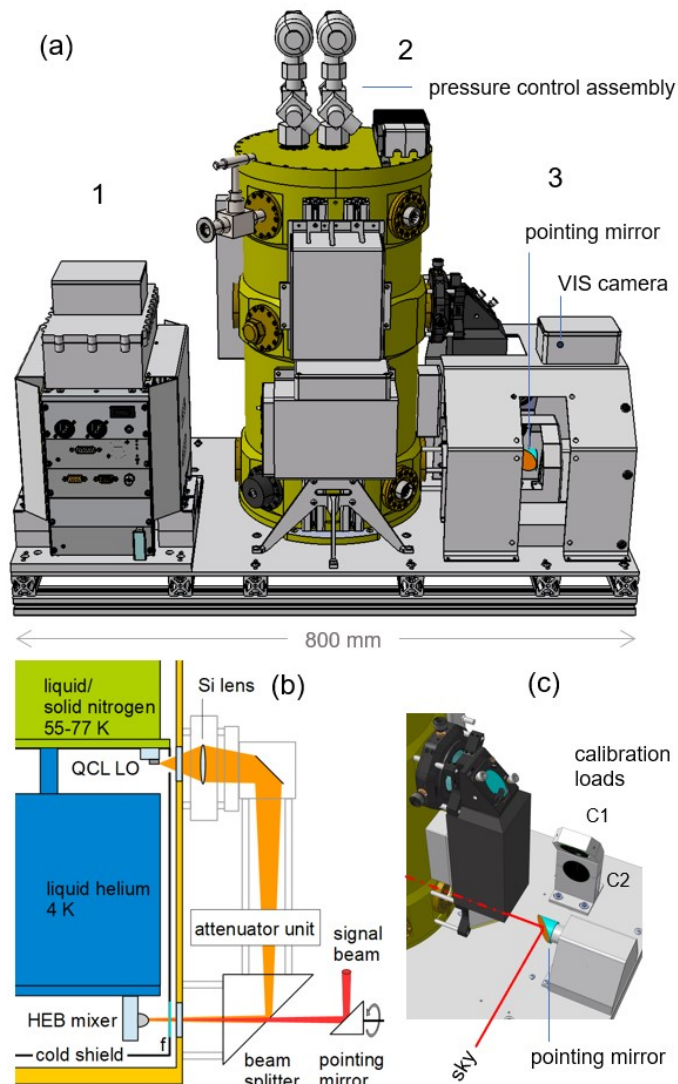

Fig. 2. (a) CAD visualization of the OSAS-B instrument. 1: main control rack with digital Fourier transform spectrometer. 2: cryostat with pressure valves and periphery control units. 3: optics compartment. (b) Schematic of the spectrometer frontend: cryostat and optics (f: cold filter). (c) Enlarged view of the optics compartment. C1 and C2 are calibration black bodies at 125 °C and ambient temperature (-32 to +23 °C at float altitude).

(Phytron, VSS 32). Calibration load C1 is a temperature-controlled (heated) groove body (triangular-shaped circular grooves resembling a multi-folded cone, 35 mm diameter). The second calibration load C2 is a solid body with a single conical cavity (30 mm aperture, 19.5° cone angle, temperature-monitored). They are made of aluminum and covered with an absorbing coating (C1: Herberts coating 1356A, C2: Nextel Suede coating 3101-90FH).

C. Hot-electron bolometer mixer

The HEB mixer comprises a 5 nm thin NbN bridge with lateral dimensions of 0.4×3 μm^2 on a high-resistivity float zone (HRFZ) Si substrate (superconducting critical temperature: $T_c = 9.7$ K). The bridge is embedded in a logarithmic spiral antenna made of Au, which also provides the electrical contacts for dc biasing and the signal at the intermediate
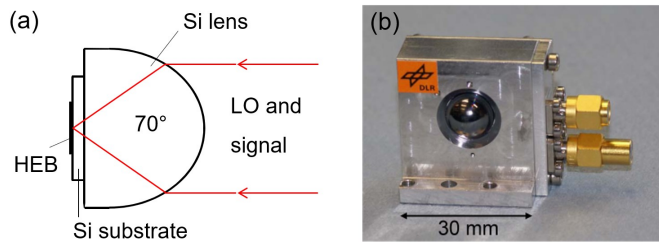
Fig. 3. Quasi-optical HEB mixer. (a) Schematic of the immersion optics. The diameter of the lens is 12 mm (6 mm curvature radius, 8.5 mm central thickness). (b) Photograph of the mounted mixer block.
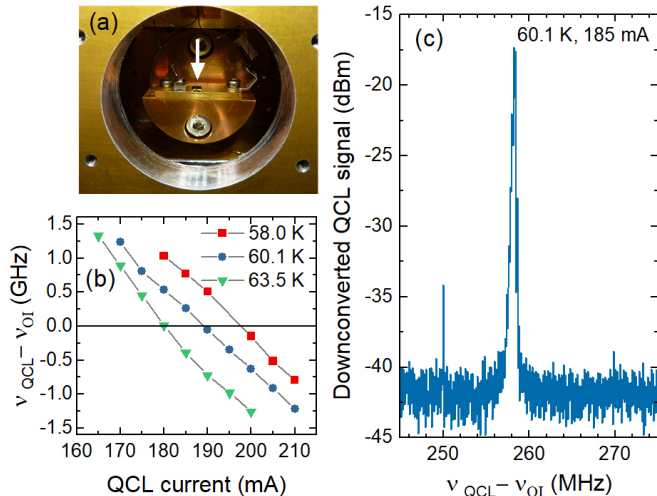

Fig. 4. (a) Photograph of the upper cryostat cavity with the mounted QCL. (b) Frequency as a function of driving current and heat sink temperature, as measured for final performance verification. $\nu_{OI} = 4.7448$ THz. (c) Downconverted QCL spectrum (resolution/video bandwidth of the spectrum analyzer: 100/11 kHz).

frequency (IF) [17], [18]. The mixer is based on a quasi-optical approach, with a lens-based immersion optics. A Si lens with parylene antireflection coating [19] is mounted on the rear side of the HEB substrate, cf. Fig. 3(a). The device is eventually assembled in a mixer block as shown in Fig. 3(b) and clamped to the 4 K cold plate. The cryogenic biasing circuit and the low-noise amplifier are directly connected via a short coaxial link. The thermal time constant of the HEB allows for a usable IF band of $0.1 - 3$ GHz.

D. Quantum-cascade laser

The QCL is based on a GaAs/AlAs active region structure, optimized toward high optical gain at low electric input power. The QCL cavity is a single-plasmon ridge waveguide with a lateral distributed-feedback grating and an additional rear-facet mirror to foster emission toward the forward direction. Details can be found in Refs. [20], [21]. For OSAS-B, the QCL is typically operated between 58–64 K. These temperatures are obtained by reducing the pressure in the nitrogen vessel to below 125 hPa, where liquid nitrogen starts to solidify. The QCL is operated in free-running mode with the electrical driving current and heat-sink temperature kept constant. The QCL produces 1–2 mW of output power at an electrical input

power of 0.6–1.0 W and covers a frequency band of several GHz around the 4.7-THz transition of OI. A picture of the QCL submount as attached to the cryostat heatsink is shown in Fig. 4(a). Figure 4(b) depicts the QCL peak frequency as a function of the driving current for three heat sink temperatures. It shows that measurements in both heterodyne sidebands, i.e. with the QCL below or above the atmospheric line, are possible. These characterizations were done with the help of a harmonic Schottky diode mixer [22], where the QCL signal is mixed with the eighth harmonic of a 593-GHz amplifier-multiplier chain (Virginia Diodes Inc.). Figure 4(c) shows an example of a down-converted spectrum as recorded with a spectrum analyzer. For an aquisition time of 0.7 s, the full-width at half maximum (FWHM) is about 350 kHz. The line width of the amplifier-multiplier chain itself is negligible, due to the low phase noise of the fundamental quartz oscillator (-130 dBc/Hz at 10 Hz). The corresponding resolving power of the spectrometer is $\nu_{OI}/\Delta\nu_{QCL} = 1.3 \times 10^7$. For comparison, the spectral width of the OI signal is 20–35 MHz (FWHM) and the in-flight integration time of a single raw spectrum is 0.25 s. Achieving a sub-MHz QCL line width has been mainly the result of eliminating noise in the supply voltage of the current driver (ppqSense, QubeCL). During flight, the drift of the QCL frequency on a longer timescale is derived from the center frequency of the OI peak in the 250 ms raw spectra. The accuracy of this method is about 0.5 MHz. For a 10 sec acquisition period, the LO frequency drift stays typically within 1 MHz.

E. Cryostat control system

The cryostat control system regulates the pressure inside the cryogen vessels via motorized valves. For a fixed pressure, the temperature of the cryogens follow the phase diagram of nitrogen and helium. For nitrogen, the triple point is at 63.2 K and 125 hPa. For pressures smaller than 125 hPa the nitrogen solidifies. Due to the absence of boiling effects, this is the preferred mode of operation for the QCL. A home-made controller measures temperature and pressure and controls the valve positions. At flight altitude the ambient pressure of about 10 hPa is sufficiently low to solidify the nitrogen, while for laboratory measurements a rotary pump is used. In order to quickly boil off the remaining cryogens prior to landing, the cryostat is equipped with additional 100 W and 5 W heaters for the nitrogen and the helium, respectively. The dimensioning of the heaters reflects the different enthalpies of vaporization.

F. Spectrometer backend

The spectrometer backend comprises an IF processor and a DFFTS with a spectral bandwidth of 1.5 GHz and 8192 channels, resulting in a bin width of 183 kHz [16]. The IF processor consists of an amplifier chain with filters and a programmable attenuator to raise the frontend IF signal level from typically -50 dBm total power after the cryogenic low-noise amplifier to the range of -30 to $+10$ dBm as required by the DFFTS. Two selectable filter routes restrict the IF pass band to the first or second Nyquist band (0–1.5 GHz and 1.5–3 GHz).

G. Instrument control and communication

Due to the complexity of the measurement, autonomous operation is limited to specific aspects such as temperature and pressure control. Remote control and monitoring of house-keeping data is maintained during the whole flight. The Hemera gondola provided a conventional internet protocol (IP) network interface for communication with the ground station via a S band radio link. The communication bandwidth is restricted to 0.1 – 1.5 MBit/s, depending on the distance between gondola and ground station and needs to be failure tolerant. All communication with the OSAS-B instrument is handled by the main on-board computer (Raspberry Pi 4), with a second unit (Raspberry Pi Zero) for redundancy. Components such as the cryostat control unit, laser driver, temperature control, mirror driver and the camera are controlled by the on-board computer via universal-serial bus (USB) interfaces. A multi-layer software based on network socket interfaces efficiently handles low-level and high-level communication. Acquired spectra and housekeeping data are saved on a local solid state drive as well as on a memory card located in a hermetically sealed housing. Most of the housekeeping data as well as integrated spectra are transferred to the ground station during flight to mitigate the risk of data loss in case the gondola cannot be recovered.

H. Power supply

Electrical power is supplied by three commercial 25.6 V LiFePO$_4$ batteries (Lithion, U1-24RT) with a total capacity of 1.5 kWh, enabling operation in excess of 12 h, as foreseen for the typical duration of return flights in the Hemera program. Batteries are thermally isolated and contained in a light-weight water proof package (total weight of 26 kg in addition to the instrument). Temperature and state of charge are monitored via a USB interface.

I. Thermal design and testing

For the thermal design and testing, two challenges had to be taken into account. First, temperature can become very low during the ascent through the tropopause and second, convective cooling is almost completely lost at flight altitude, where air density is less than 1% of the ground level. The total power consumption and heat dissipation of the instrument is approximately 90 W in full operation, with the largest heat load being the DFFTS (ca. 35 W). To tackle the first problem, individual components of the instrument had been tested at ambient temperatures down to -75°C. Heaters were added to those components that are not specified for such temperatures and showed a tendency to fail. For solving the second problem – avoid over-heating at flight altitude – all heat sinking was designed toward the base plate of the instrument and the gondola frame providing a sufficiently large mass and heat capacity to prevent overheating during a one-day flight. Eventually, several test runs with the instrument in a thermal vacuum chamber had been performed. Besides qualification of the instrument for the harsh stratospheric conditions, these test runs were further used for the radiometric performance verification.
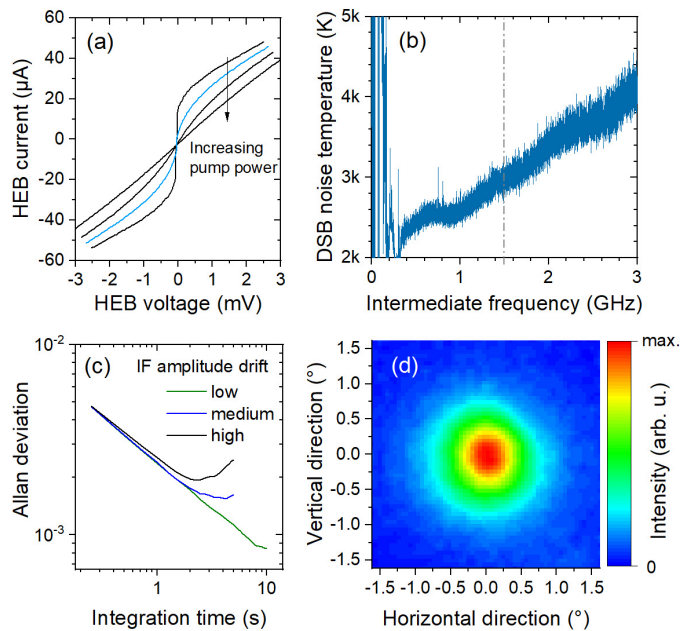

Fig. 5. (a) HEB characteristics under variation of the pump intensity. (b) DSB noise temperature as a function of the frequency. The dashed line separates the two Nyquist bands (0 – 1.5 GHz, 1.5 – 3.0 GHz) which were measured subsequently. Temperature of hot (cold) load: 400 K (94 K). (c) Allan deviation of the IF spectral power density (bin width: 183 kHz) for different drift situations due to sun exposure and gondola rotation. (d) Measured receiver beam profile.

J. Receiver characterization and performance

For heterodyne operation, the HEB mixer is pumped by the QCL LO close to the superconducting transition temperature. Figure 5(a) depicts the dc current-voltage characteristic of the HEB for a variation of the pump power. The characteristic corresponding to optimum receiver sensitivity (minimum noise temperature) is highlighted by blue color, with the sensitivity optima at $+0.5$ and -0.5 mV.

Figure 5(b) shows the double-side-band (DSB) noise temperature as obtained from calibration load measurements. The calculation follows the standard approach, cf. Eq. (2) of the Appendix and does not take into account the direct detection effect [23]–[25]. A noise temperature optimum is obtained for an IF range of 0.4 – 1 GHz. Below 0.4 GHz, the sensitivity is limited by insufficient gain of the amplifier chain and above 1 GHz by the thermal time constant of the HEB mixer [17]. The radiometric calibration, single- and double-side-band detection as well as the direct-detection effect for HEB mixers are briefly discussed in the Appendix. Corrections for the radiometric calibration from the direct-detection effect will be treated in detail in a separate publication [26].

As for any receiver, the optimum integration time is eventually limited by drift effects. Figure 5(c) depicts the Allan plot for the amplitude stability of the IF signal for three in-flight drift situations. The inherent rotation of the gondola in combination with sun exposure limits the Allan time to typically 2 to 10 sec during flight.

Figure 5(d) depicts the receiver beam profile as obtained from raster scans of a hot-spot source at a distance of 1.1 m
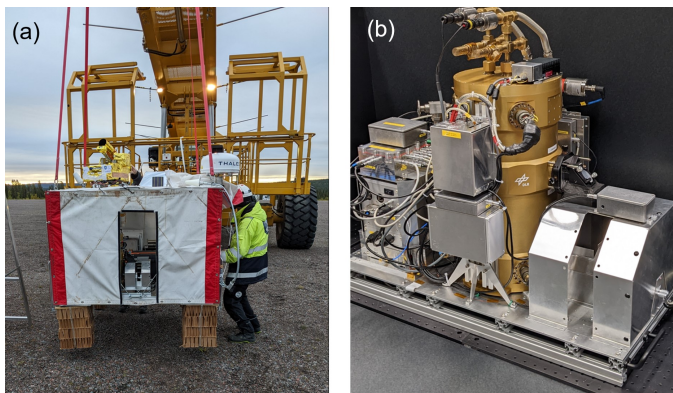
Fig. 6. (a) Gondola prior to launch. OSAS-B is looking frontward through the canvas outcut. (b) OSAS-B instrument after recovery and re-validation.
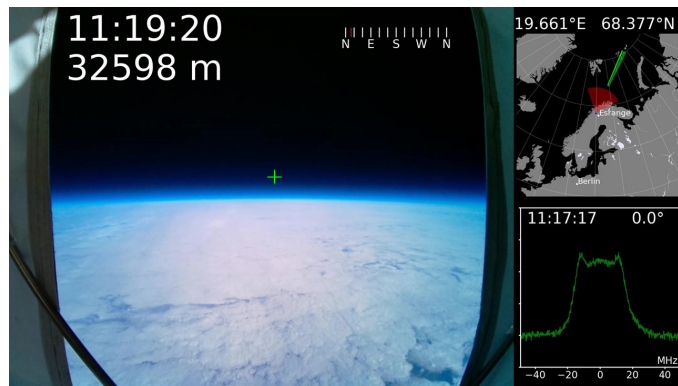

Fig. 7. Camera image and the orientational data during flight. Left panel: onboard camera picture with local time, flight altitude and azimuth information. The cross illustrates the pointing of the spectrometer. Upper right panel: map with the actual position, camera field of view (red) and line of sight of the spectrometer (green). Lower right panel: acquired OI spectrum along the line of sight shown in the upper panel, local time of the measurement and elevation angle.

from the mixer. For such measurements, the total power of the IF signal was recorded for each position of the source. The hot-spot source is formed by a 1000 °C blackbody behind a circular room-temperature aperture (15 mm diameter). The figure shows an almost Gaussian profile with a FWHM divergence of 0.85° in horizontal and 0.90° in vertical direction. Taking into account the convolution with the finite size of the aperture, the pure receiver beam divergence becomes 0.60° and 0.65°, respectively.

III. BALLOON FLIGHT IN SEPTEMBER 2022

The flight with a zero pressure balloon took place on Sept. 7th, 2022 from Esrange/Kiruna in Sweden with a launch at 7:19 local time (5:19 UTC). Figure 6(a) shows the gondola prior to launch with the outcut in the protecting canvas for the OSAS-B instrument. After an ascent of 1.5 h, an altitude of 32.5 km was reached and maintained for 4 h. After that, due to an unfavorable wind direction, an altitude of 25 km was approached and maintained for another 4 h. OI measurements were made from 8:30 to 17:00 local time. The flight was terminated at 18:14 local time about 100 km apart from the launch site. Despite a rather hard landing on rocky ground, the mechanical shock was fully absorbed by the semi-rigid support structure and the actual instrument could be recovered with negligible damage. Figure 6(b) shows the OSAS-B instrument after recovery and re-validation, which did not show any degradation of the instrument performance.

Note that the azimuth view direction could be tracked but not controlled, since the gondola did not feature azimuth pointing control. In order to determine the azimuth direction, OSAS-B is equipped with an electronic compass and a camera mounted above the pointing mirror. Geolocation and altitude are provided by the balloon piloting system. Figure 7 shows the camera image and the orientation data collected during the flight (also available as a video). The exemplary OI spectrum in the lower right panel corresponds to the projected line of sight in the upper right map.

The inherent rotation of the gondola enabled data acquisition for most directions during the course of the flight. Figure 8(a) shows the flight trajectory and the projected lines of sight for the acquired spectra. Figure 8(b) depicts the azimuth view
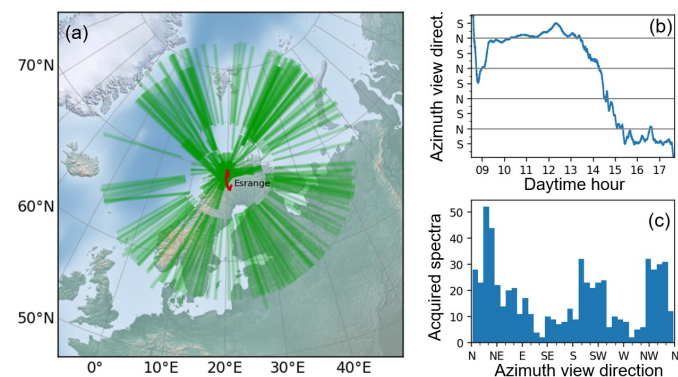

Fig. 8. (a) Map with flight trajectory in red and projected lines of sight in green color. Lines of sight are plotted for the height range of 50 – 200 km, where more than 97% of the atomic oxygen resides. (b) Azimuth view direction during the course of the flight. (c) Histogram of the view directions (10° binning). North (N) corresponds to an azimuth angle of 0°, south (S) to 180°.

direction during the course of the flight illustrating the gondola rotation with varying angular velocity (up to the degree-per-second range). A histogram of the azimuth directions is shown in Fig. 8(c). The azimuth view direction is of particular importance at low elevation angles, for which the geographic latitude and longitude varies substantially along the line of sight.

Raw spectra were acquired with an integration time of 250 ms. A measurement sequence consists of typically 20/20/40 raw spectra (corresponding to 5/5/10 s integration time) with the receiver pointing subsequently to each of the two calibration loads and to the sky. Integrated spectra were evaluated in-flight to monitor the receiver noise temperature and to preview atmospheric spectra. For post-flight data processing and merging, each raw spectrum and each housekeeping datum contains a timestamp with millisecond resolution. There had been a continuous surveillance of operational parameters during flight. Once an increase of noise temperature, a drift of the HEB operating point, or a too large or too small IF power level was found, measurements were
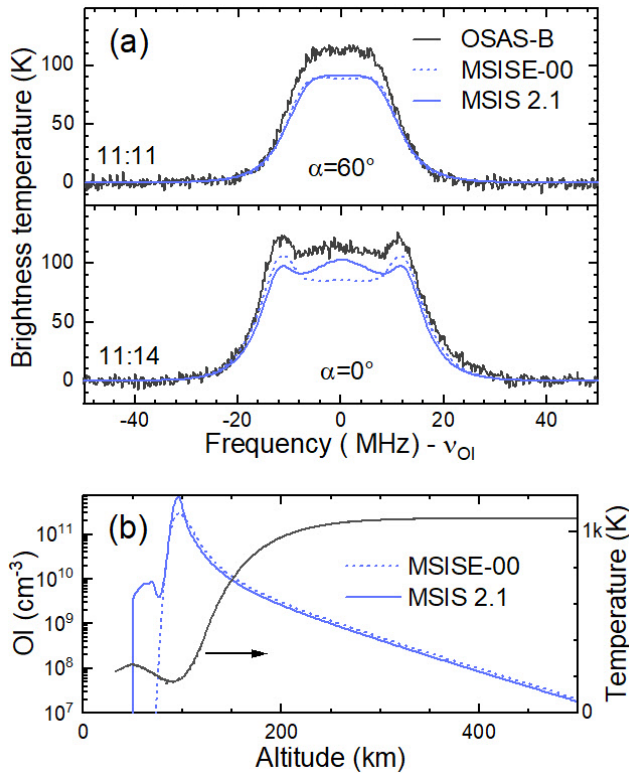
Fig. 9. (a) Measured and simulated spectra at 60° elevation (upper panel) and 0° elevation (lower panel) with preliminary intensity calibration. The atmospheric integration time is 10 s and the spectral bin width is 183 kHz. Simulated spectra are based on the NRL MSISE-00 (dashed blue line) and the MSIS 2.1 model (solid blue line). Azmiuth pointing was 23°. (b) OI concentration and temperature profile in the MLT according to the NRLMSISE-00 and MSIS 2.1 model. Note the differences below 80 km.
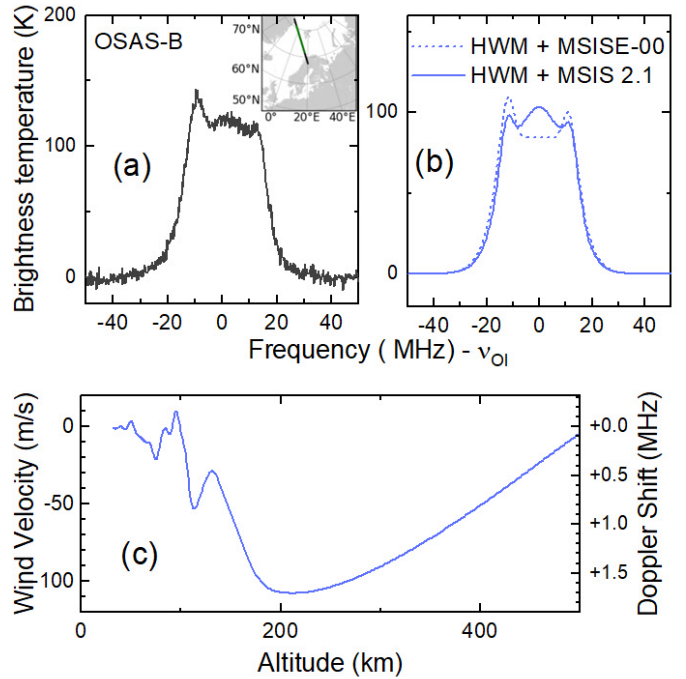

Fig. 10. (a) Measured asymmetric OI spectrum (preliminary intensity calibration). The inset map depicts the line of sight projection. Local time: 9:36, elevation: 0°, azimuth pointing: 342° (b) Simulated spectra including the wind-related Doppler shift. Same spatial-temporal conditions as in (a). (c) Wind velocitiy along the line of sight according to the HWM-2014 model and corresponding Doppler shift.

stopped, to adjust the optical attenuation of the LO power (typically four times per hour), HEB bias and IF amplification. A certain drift of the LO power is expected due to the rotating gondola and the optical alignment of the QCL beam, which depends on the thermal expansion and contraction of the cryostat with the ambient temperature at float altitude (-32 to +23°C). In total, more than 50,000 raw spectra were acquired resulting in about 620 integrated OI spectra during the course of the flight.

IV. First scientific results

Figure 9(a) shows two spectra for 60° and 0° elevation, measured in the late morning in north-eastern direction. The spectrum for 0° elevation exhibits a pronounced wing structure. This wing structure is due to an interplay of emission and absorption from different altitudes, and reflects the radiation transport in the MLT region. The blue lines represent radiation transfer calculations based on the concentration and temperature profile predicted by the NRL MSISE-00 model (US Naval Research Laboratory Mass Spectrometer and Incoherent Scatter Radar Exosphere - 2000) [27] and the more recent MSIS 2.1 model [28]. The two models differ mainly in the atomic-oxygen concentration below 80 km as depicted in Fig. 9(b). Although the differences are very subtle, they change the shape of the OI spectra in a way which is observable with

OSAS-B, due to its high sensitivity and spectral resolution. In more detail, the central peak in the measured spectrum at 0° elevation is caused by the atomic oxygen maximum at 70 km altitude. This demonstrates that the measured spectra contain detailed altitude information of atomic oxygen and allow for distinguishing between atmospheric models of the MLT. Although the radiometric calibration is preliminary, the agreement between the measured and expected brightness temperature of the OI line is in a reasonable range.

Many of the measured spectra are found to be slightly asymmetric. An example is shown in Fig. 10(a). It turned out that these asymmetries are explained by high-altitude shear winds, which result in a relative Doppler shift between spectral components from different altitudes. Such shear winds are predicted by the horizontal-wind model (HWM) for the MLT [29], [30]. Note that during flight there is no frequency reference except the OI line itself. For that reason, the absolute Doppler shift of the center frequency cannot be determined, but this does not hold for the relative shift of spectral components due to wind gradients. Figure 10(b) shows the result of a radiative transfer calculation including the wind-caused Doppler shift along the line of sight [Fig. 10(c)]. The qualitative agreement to Fig. 10(a) illustrates the sensitivity of heterodyne spectroscopy to wind velocity gradients in the MLT.

V. Summary and Outlook

The OSAS-B instrument was developed to study atomic oxygen in the MLT of the Earth. The approach has the advan-

tage of being substantially less expensive than a comparable satellite mission, while being not affected by residual water vapor absorption as for an aircraft instrument. The results from the first flight demonstrate the high scientific potential of such a balloon-borne heterodyne spectrometer with cryogenic front end. More compact, cryogen-free instruments for longer missions might be based on Schottky diodes as mixers [31], though these are currently not available at 4.7 THz and have to deal in general with a substantially smaller sensitivity as compared to cryogenic mixers. The robust design and reliable performance of OSAS-B will enable systematic studies with respect to diurnal and annual variations as well as geolocation. Operating such an instrument in a gondola with azimuth pointing control, absorption measurements against the sun or the moon become feasible. This will allow for direct column density measurements and for studying less abundant oxygen isotopes [10].

APPENDIX: DATA EVALUATION

In this section, we briefly describe the physical and mathematical background for obtaining emission spectra from raw spectral data.

The spectral power P_S of the incoming signal radiation is a function of temperature $P_S=P_S(T)$ according to Planck's law. For simplicity, we use the Rayleigh-Jeans temperature (or brightness temperature) J, which is proportional to the radiated power within a certain band: $P = k_B J \Delta\nu$. The detected IF power of a blackbody corresponds to

$$P_{\mathrm{IF}} = G(J_S + J_N) , \qquad (1)$$

where G denotes the gain factor and $J_N = P_N/G$ the mixer noise temperature. For constant G and J_N, the noise temperature can be determined with the help of two blackbodies with known temperature, in the following hot and cold load (subscripts H, C).

$$J_N = \frac{J_H - Y J_C}{Y - 1} , \qquad (2)$$

with $Y = P_H/P_C$. The Rayleigh-Jeans temperature of an unknown blackbody S can be determined by:

$$J_S = \frac{P_S(J_H - J_C) + P_H J_C - P_C J_H}{P_H - P_C} . \qquad (3)$$

The physical temperature of the blackbody can be determined with the help of Planck's law by

$$T = \frac{h\nu}{k_B \ln(\frac{h\nu}{k_B J} + 1)} \qquad (4)$$

and vice versa

$$J = \frac{h\nu}{k_B} \frac{1}{\exp(h\nu/(k_B T)) - 1} , \qquad (5)$$

where ν is the frequency and k_B the Boltzmann constant. This equation corresponds to Planck's law with a one-dimensional density of states as it is valid for the mixer device. One immediate consequence is that the minimum detectable temperature depends on the frequency. A physical temperature of 50 K

corresponds to a brightness temperature of 0.1 K at 4.7 THz, since almost no photons are emitted.

For a DSB receiver, the received emission of a calibration blackbody adds to both side bands. For a narrow spectral source, such as the OI emission, which appears only in the upper or in the lower side-band this has to be taken into account. Assuming the same gain for both side bands (side band ratio of unity), the brightness temperature resulting from Eq. (3) has to be multiplied by two. Note that Eq. (3) does not take into account the direct response of the HEB to blackbody radiation. If the change of the bolometer temperature due to the direct response becomes large enough, it affects the heterodyne gain and to a certain extent the mixer noise floor. For OSAS-B, the respective radiometric correction reduces the amplitude by of about 30%. A general model for HEB mixers which yields the radiometric calibration by taking into account the direct response as well as potential zero-point fluctuations will be published separately [26].

REFERENCES

[1] M. Riese, D. Offermann, and G. Brasseur, "Energy released by recombination of atomic oxygen and related species at mesopause heights," *J. Geophys. Res.*, vol. 99, no. D7, pp. 14 585–14 593, 1994.

[2] M. G. Mlynczak and S. Solomon, "A detailed evaluation of the heating efficiency in the middle atmosphere," *J. Geophys. Res.*, vol. 98, no. D6, pp. 10 517–10 541, 1993.

[3] J. T. Emmert, J. M. Picone, and R. R. Meier, "Thermospheric global average density trends, 1967–2007, derived from orbits of 5000 near-Earth objects," *Geophys. Res. Lett.*, vol. 35, no. 5, p. L05101, 2008.

[4] M. Shan, J. Guo, and E. Gill, "Review and comparison of active space debris capturing and removal methods," *Prog. Aerosp. Sci.*, vol. 80, pp. 18–32, 2016.

[5] Q. Wu, R. D. Gablehouse, S. C. Solomon, T. L. Killeen, and C.-Y. She, "A new Fabry-Perot interferometer for upper atmosphere research," in *Proc. SPIE*, vol. 5660, 2004, pp. 218 – 227.

[6] K. Moe and Q. Wu, "Impact of HIWIND balloon measurements on thermospheric density models," *J. Geophys. Res.*, vol. 119, no. 4, pp. 2476–2483, 2014.

[7] A. K. Smith, D. R. Marsh, M. G. Mlynczak, and J. C. Mast, "Temporal variations of atomic oxygen in the upper mesosphere from SABER," *J. Geophys. Res.*, vol. 115, no. D18, p. D18309, 2010.

[8] C. Risacher, R. Güsten, J. Stutzki, H.-W. Hübers, D. Büchel, U. U. Graf, S. Heyminck, C. E. Honingh, K. Jacobs, B. Klein, T. Klein, C. Leinz, P. Pütz, N. Reyes, O. Ricken, H.-J. Wunsch, P. Fusco, and S. Rosner, "First supra-THz heterodyne array receivers for astronomy with the SOFIA observatory," *IEEE Trans. Terahertz Sci. Technol.*, vol. 6, no. 2, pp. 199–211, 2016.

[9] H. Richter, C. Buchbender, R. Güsten, R. Higgins, B. Klein, J. Stutzki, H. Wiesemeyer, and H.-W. Hübers, "Direct measurements of atomic oxygen in the mesosphere and lower thermosphere using terahertz heterodyne spectroscopy," *Commun. Earth Environ.*, vol. 2, no. 1, p. 19, 2021.

[10] H. Wiesemeyer, R. Güsten, R. Aladro, B. Klein, H.-W. Hübers, H. Richter, U. U. Graf, M. Justen, Y. Okada, and J. Stutzki, "First detection of the atomic ^{18}O isotope in the mesosphere and lower thermosphere of Earth," *Phys. Rev. Res.*, vol. 5, p. 013072, 2023.

[11] C. Walker, C. Kulesa, A. Young, W. Verts, J.-R. Gao, Q. Hu, J. Silva, B. Mirzaei, W. Laauwen, J. Hesler, C. Groppi, and A. Emrich, "Gal/Xgal U/LDB Spectroscopic/Stratospheric THz Observatory: GUSTO," in *Proc. SPIE*, vol. 12190, 2022, p. 121900E.

[12] J. L. Kloosterman, D. J. Hayton, Y. Ren, T. Y. Kao, J. N. Hovenier, J. R. Gao, T. M. Klapwijk, Q. Hu, C. K. Walker, and J. L. Reno, "Hot electron bolometer heterodyne receiver with a 4.7-THz quantum cascade laser as a local oscillator," *Appl. Phys. Lett.*, vol. 102, no. 1, p. 011123, 2013.

[13] D. E. Kelleher, W. C. Martin, W. L. Wiese, J. Sugar, J. R. Fuhr, K. Olsen, A. Musgrove, P. J. Mohr, J. Reader, and G. R. Dalton, "The new NIST atomic spectra database," *Phys. Scr.*, vol. 1999, no. T83, p. 158, 1999.

[14] F. Friedl-Vallon, K. Dannenberg, P. Raizonville, and A. Vargas, "Stratospheric balloons: low-cost platforms for science and technology development," in *Proc. SPIE*, vol. 11180, 2019, p. 111807J.

[15] (2021) Hemera 2020 website. [Online]. Available: https://www.hemera-h2020.eu

[16] Klein, B., Hochgürtel, S., Krämer, I., Bell, A., Meyer, K., and Güsten, R., "High-resolution wide-band fast Fourier transform spectrometers," *A&A*, vol. 542, p. L3, 2012.

[17] A. D. Semenov, H.-W. Hübers, J. Schubert, G. N. Gol'tsman, A. I. Elantiev, B. M. Voronov, and E. M. Gershenzon, "Design and performance of the lattice-cooled hot-electron terahertz mixer," *J. Appl. Phys.*, vol. 88, no. 11, pp. 6758–6767, 2000.

[18] A. D. Semenov, H. Richter, H.-W. Hubers, B. Gunther, A. Smirnov, K. S. Il'in, M. Siegel, and J. P. Karamarkovic, "Terahertz performance of integrated lens antennas with a hot-electron bolometer," *IEEE Trans. Microw. Theory Tech.*, vol. 55, no. 2, pp. 239–247, 2007.

[19] H.-W. Hübers, J. Schubert, A. Krabbe, M. Birk, G. Wagner, A. Semenov, G. Gol'tsman, B. Voronov, and E. Gershenzon, "Parylene anti-reflection coating of a quasi-optical hot-electron-bolometric mixer at terahertz frequencies," *Infrared Phys. Technol.*, vol. 42, no. 1, pp. 41–47, 2001.

[20] T. Hagelschuer, H. Richter, M. Wienold, X. Lü, B. Röben, L. Schrottke, K. Biermann, H. T. Grahn, and H.-W. Hübers, "A compact 4.75-THz source based on a quantum-cascade laser with a back-facet mirror," *IEEE Trans. Terahertz Sci. Technol.*, vol. 9, no. 6, pp. 606–612, 2019.

[21] L. Schrottke, X. Lü, B. Röben, K. Biermann, T. Hagelschuer, M. Wienold, H.-W. Hübers, M. Hannemann, J.-P. H. van Helden, J. Röpcke, and H. T. Grahn, "High-performance GaAs/AlAs terahertz quantum-cascade lasers for spectroscopic applications," *IEEE Trans. Terahertz Sci. Technol.*, vol. 10, no. 2, pp. 133–140, 2020.

[22] D. Jayasankar, V. Drakinskiy, N. Rothbart, H. Richter, X. Lü, L. Schrottke, H. T. Grahn, M. Wienold, H.-W. Hübers, P. Sobis, and J. Stake, "A 3.5-THz, ×6-harmonic, single-ended Schottky diode mixer for frequency stabilization of quantum-cascade lasers," *IEEE Trans. Terahertz Sci. Technol.*, vol. 11, no. 6, pp. 684–694, 2021.

[23] J. Baselmans, M. Hajenius, J. Gao, A. Baryshev, J. Kooi, T. Klapwijk, B. Voronov, P. de Korte, and G. Gol'tsman, "NbN hot electron bolometer mixers: sensitivity, LO power, direct detection and stability," *IEEE Trans. Appl. Supercond.*, vol. 15, no. 2, pp. 484–489, 2005.

[24] J. J. A. Baselmans, A. Baryshev, S. F. Reker, M. Hajenius, J. R. Gao, T. M. Klapwijk, Y. Vachtomin, S. Maslennikov, S. Antipov, B. Voronov, and G. Gol'tsman, "Direct detection effect in small volume hot electron bolometer mixers," *Appl. Phys. Lett.*, vol. 86, no. 16, p. 163503, 2005.

[25] A. Shurakov, Y. Lobanov, and G. Gol'tsman, "Superconducting hot-electron bolometer: from the discovery of hot-electron phenomena to practical applications," *Supercond. Sci. Technol.*, vol. 29, no. 2, p. 023001, 2015.

[26] A. Semenov, M. Wienold, M. Sidorova, and H.-W. Hübers, *submitted to J. Appl. Phys.*, 2024.

[27] J. M. Picone, A. E. Hedin, D. P. Drob, and A. C. Aikin, "NRLMSISE-00 empirical model of the atmosphere: Statistical comparisons and scientific issues," *J. Geophys. Res.*, vol. 107, no. A12, p. 1468, 2002.

[28] J. T. Emmert, M. Jones Jr, D. E. Siskind, D. P. Drob, J. M. Picone, M. H. Stevens, S. M. Bailey, S. Bender, P. F. Bernath, B. Funke, M. E. Hervig, and K. Pérot, "NRLMSIS 2.1: An empirical model of nitric oxide incorporated into MSIS," *J. Geophys. Res.*, vol. 127, no. 10, p. e2022JA030896, 2022.

[29] M. Dhadly, F. Sassi, J. Emmert, D. Drob, M. Conde, Q. Wu, J. Makela, S. Budzien, and A. Nicholas, "Neutral winds from mesosphere to thermosphere—past, present, and future outlook," *Front. Astron. Space Sci.*, vol. 9, 2023.

[30] D. P. Drob, J. T. Emmert, J. W. Meriwether, J. J. Makela, E. Doornbos, M. Conde, G. Hernandez, J. Noto, K. A. Zawdie, S. E. McDonald, J. D. Huba, and J. H. Klenzing, "An update to the horizontal wind model (HWM): The quiet time thermosphere," *Earth Space Sci.*, vol. 2, no. 7, pp. 301–319, 2015.

[31] D. L. Wu, J.-H. Yee, E. Schlecht, I. Mehdi, J. Siles, and B. J. Drouin, "THz limb sounder (TLS) for lower thermospheric wind, oxygen density, and temperature," *J. Geophys. Res. Space Physics*, vol. 121, no. 7, pp. 7301–7315, 2016.